



ORIGINAL PAPER

Sheng Li · Chen-Yuan Bai · Zi-Niu Wu

# Nonlinear supersonic indicial response of diamond airfoils

Received: 2 August 2019 / Revised: 26 January 2020 / Published online: 5 March 2020  
© Springer-Verlag GmbH Austria, part of Springer Nature 2020

**Abstract** Supersonic flows around diamond airfoils, under large-amplitude step motion, are analytically studied. Nine regions with distinct flow structures are identified on each side. These regions include intricate wave structures and significantly shape the indicial response. The novelty of this work is to develop theoretical models, capable of describing each region's wave speed, pressure, and force. We achieve this by correcting the linear solution to the problem and incorporating nonlinear effects of large angle and airfoil thickness. Our model reports good accuracy regarding the computational fluid dynamics. And three stages, which are predicted by this model, precisely capture important features of aerodynamic force evolution.

## 1 Introduction

Indicial response is a paramount issue in unsteady aerodynamics. It reflects the aerodynamic force evolution after a sudden change in the angle of attack (AoA) and speed. It has broad applications in aeroelasticity [1, 2] and aircraft control [3–5]. For arbitrary motions of aircraft, this model is also of great value. As suggested by Tobak [6], these arbitrary motions could be decomposed into a sequence of step motions. Via Duhamel integration or Volterra theory, aerodynamic forces can be analytically presented.

The investigation of supersonic indicial response is traced back to Heaslet and Lomax [7]. They investigated small-amplitude step motion of a flat plate and found three regions on the each side, as visualized in Fig. 1a. They [7] derived linear solutions to each region by potential flow theory and further extended them to three-dimensional cases [8]. Bisplinghoff [1] adopted Laplace transforms to derive an alternative indicial function to this problem. Jaworski [9] considered airfoil downwash of arbitrary profiles in supersonic flow and derived quadrature indicial lift functions.

For large-amplitude step motions, nonlinear effects become crucial. The onset of shock waves and rarefaction waves makes linear theory incompetent to give accurate indicial responses. To reveal nonlinear flow physics, Bai and Wu [10] carried the research of flat plate. They found that, after large-amplitude step motion, three regions are also on each side. As shown in Fig. 1b, on the windward, Region I is covered by a steady oblique shock wave and Region III is covered by an unsteady normal shock wave; on the leeward, Region I is covered by a Prandtl–Meyer wave, and Region III is covered by a moving rarefaction wave. As for Region II, there are curved shock wave and curved rarefaction wave, respectively. In their later paper [11], Bai and Wu

---

S. Li · C.-Y. Bai · Z.-N. Wu  
School of Aerospace Engineering, Tsinghua University, Beijing, China  
E-mail: leesheng\_thu@outlook.com

C.-Y. Bai  
E-mail: baichenyuan@sina.com

Z.-N. Wu  
E-mail: ziniuwu@tsinghua.edu.cn

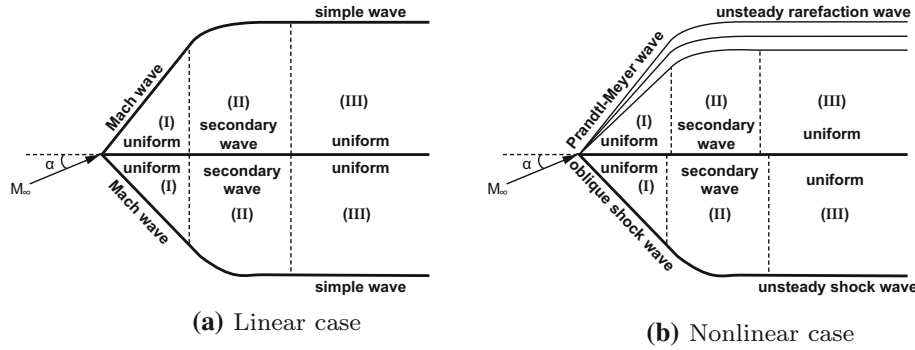


**Fig. 1** Flow structure of the plate after step motion [10]

unveiled that the essence of Region II is a two-dimensional Riemannian flow problem. They are nonuniform, and time dependent, and thus it is hard to obtain analytical solutions directly. Bai and Wu [10] used a correction method to obtain nonlinear solutions for each region. They retained the form of linear solutions and updated flow parameters by nonlinear solutions to shock waves and rarefaction waves. This model is proven reasonably accurate by numerical results. Further applications [12,13] show that this model can serve well as the kernel function of Duhamel integration and predict nonlinear aerodynamic force of general motions.

However, previous discussions are restricted to zero thickness assumption. This is not the case for general airfoils. In fact, thickness effects will induce complex interactions between nonlinear waves and Mach waves [14] and further change the indicial response. To achieve understanding of its mechanism and build a corresponding nonlinear model, we investigate diamond airfoils in this paper. For simplicity, inviscid flow is assumed, and thus the windward and the leeward can have independent supersonic indicial response. The derived model incorporates nonlinear effects of two regimes: large-amplitude motion and airfoil thickness. Our analysis demonstrates that the presence of thickness contributes to more regions and secondary wave structures of new types, and shapes the supersonic indicial response into three stages.

The remaining Sections are arranged as follows. In Sect. 2, the linear solution of a flat plate and its nonlinear correction are recalled, providing a methodology base for our research. In Sect. 3, we derive the linear supersonic indicial response of a diamond airfoil. In Sect. 4, we clarify the flow structure for the nonlinear case and adapt the linear solution for large-amplitude motion and airfoil thickness, according to three stages in the process. In Sect. 5, a validation via computational fluid dynamics is carried out, and the effect of thickness is discussed. In Sect. 6, the conclusion and comments are given.

## 2 Review of supersonic indicial response of a flat plate

The supersonic indicial response of a flat plate has been investigated by using the linear theory [7] and by the nonlinear correction method [10], which are instructional to our research of a diamond airfoil. Here is a brief review of related methods and results.

### 2.1 Linear solution by Heaslet and Lomax

Heaslet and Lomax's linear solution [7] is based on the linear potential flow model. The perturbation by plate is assumed small compared with freestream. In the flow-fixed frame, the equation of the perturbed potential  $\varphi$  is of the following form:

$$\varphi_{xx} + \varphi_{yy} = \varphi_{t't'}, \quad t' = a_\infty t. \quad (1)$$

Heaslet and Lomax deemed  $t'$  as another spatial coordinate. Thus, a time-marching process could be reflected by a three-dimensional steady problem. By Fig. 2, they reported three regions' existence. Region I and Region III are out of Mach cones (marked with dash line), representing the uniform regions already affected or unaffected by the leading edge. Steady Mach waves and unsteady Mach waves cover them, respectively. Region II is where adjacent regions interact, actually a secondary wave region with nonuniform pressure distribution. By placing sources, they derived an analytical solution to each region. For later use, we list the

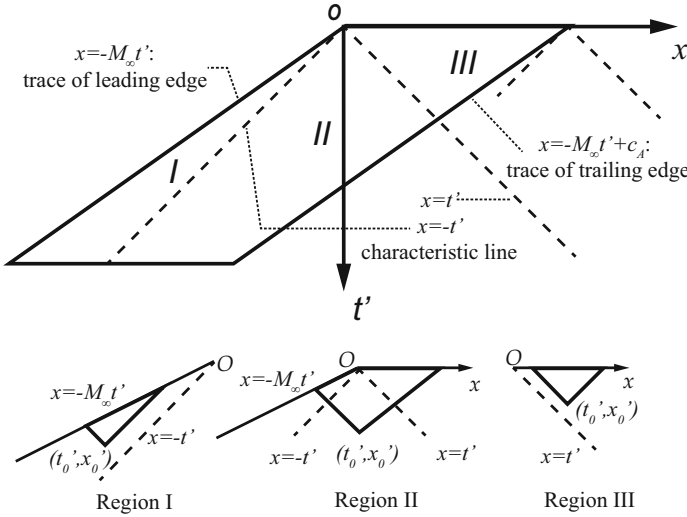


**Fig. 2** Regions of the flat plate in  $x - t'$  plane

versions adopted by Bai and Wu [10] here. They are based on a body-fixed frame and can be proved equivalent to the original forms.

Let  $\alpha$  be AoA and  $xl = (U_\infty - a_\infty)t$  and  $xr = (U_\infty + a_\infty)t$  be the demarcation lines of regions. For Region I( $\in [0, xl]$ ) and Region III( $\in [xr, c_A]$ ):

$$Cp_I = \pm \frac{2\alpha}{\sqrt{M_\infty^2 - 1}}, \quad Cp_{III} = \pm \frac{2\alpha}{M_\infty}. \quad (2)$$

Here, ‘+’ is for the windward; ‘-’ is for the leeward. For secondary wave regions ( $\in (xl, xr)$ ), let

$$U_\infty t = \frac{xr + xl}{2}, \quad a_\infty t = \frac{xr - xl}{2}, \quad M_\infty = \frac{xr + xl}{xr - xl}. \quad (3)$$

The solution to Region II can be written as:

$$Cp_{II} = Cp_I \frac{1}{\pi} \arccos \eta + Cp_{III} \frac{1}{\pi} \left( \frac{\pi}{2} + \arcsin \xi \right) \quad (4)$$

where:

$$\begin{cases} \xi = \frac{2x - (xl + xr)}{xr - xl} \\ \eta = \frac{1}{x} \left( \frac{xl + xr}{xr - xl} \left( x - \frac{xl + xr}{2} \right) + \frac{xr - xl}{2} \right). \end{cases} \quad (5)$$

## 2.2 Nonlinear correction by Bai and Wu

In the nonlinear case, as illustrated in Fig. 1b, similar ‘uniform–nonuniform–uniform’ regions are on both sides. With the increase in AoA, nonlinear waves replace original Mach waves, with oblique shock wave (Region I) and unsteady normal shock wave (Region III) on the windward, and Prandtl–Meyer wave (Region I) and unsteady rarefaction wave (Region III) on the leeward. Their solutions are shown in the “Appendix.”

For Region II, the onset of a curved shock wave and a curved expansion wave makes it difficult to attain an analytical solution. Bai and Wu [10] assumed an analogous distribution to that of the linear case. They made nonlinear substitutes for pressure coefficients and boundaries in Eq. (4). For the windward,

$$Cp_{II}^{(W)} = Cp_I^{(W)} \frac{1}{\pi} \arccos \eta^{(W)} + Cp_{III}^{(W)} \frac{1}{\pi} \left( \frac{\pi}{2} + \arcsin \xi^{(W)} \right). \quad (6)$$

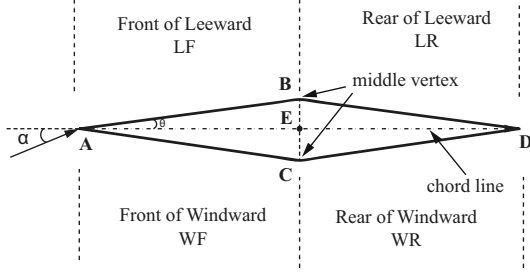


**Fig. 3** Denotation

**Table 1** Equivalent AoA for each surface

Surface	WF	WR	LF	LR
Equivalent AoA	$\alpha + \theta$	$\alpha - \theta$	$\theta - \alpha$	$-(\alpha + \theta)$

Here:

$$\begin{cases} \xi^{(W)} = \frac{2x - (xl^{(W)} + xr^{(W)})}{xr^{(W)} - xl^{(W)}} \\ \eta^{(W)} = \frac{1}{x} \left( \frac{xl^{(W)} + xr^{(W)}}{xr^{(W)} - xl^{(W)}} \left( x - \frac{xl^{(W)} + xr^{(W)}}{2} \right) + \frac{xr^{(W)} - xl^{(W)}}{2} \right). \end{cases} \quad (7)$$

Superscript W denotes nonlinear solutions in the windward. And  $xl^{(W)} = (u_I^{(W)} - a_I^{(W)})t$  and  $xr^{(W)} = (u_{III}^{(W)} + a_{III}^{(W)})t$ . For the leeward, the correction is similar. Expressions are therefore omitted here.

### 3 Linear supersonic indicial response for diamond airfoils

This Section includes our derivation of linear response to diamond airfoils, based on methods and results in Sect. 2.1. Nine regions are found forming after the step motion, and our models analytically predict their boundaries and pressure distribution.

#### 3.1 Denotations

For a diamond airfoil illustrated in Fig. 3, we use superscripts W and L to denote its windward and leeward, and set AoA and half vertex angle to be  $\alpha$  and  $\theta$ , respectively. Surfaces of the airfoil are marked by WF, WR, LF, and LR according to their position. Their equivalent AoA is listed in Table 1. Two body-fixed frames—Coord F and Coord R—are set at Point A and Point E, respectively, with both x axes along the chord line. To avoid confusion, we distinguish them with subscripts F and R.

#### 3.2 Derivation

Since the windward and the leeward have separate supersonic indicial responses, we only exemplify the derivation of windward solutions here. For the leeward, its solutions are of the same form but different in pressure coefficients and equivalent AoA.

Following Heaslet and Lomax [7], we place sources of strength  $q_{WF} = 2V_\infty \alpha_{WF}$  in WF and  $q_{WR} = 2V_\infty \alpha_{WR}$  in WR.  $\alpha_{WF}$  and  $\alpha_{WR}$  can be found in Table 1. A sketch, similar to Fig. 2, can be accordingly drawn (see Fig. 4). It can be seen that Mach cones and the trace of middle vertex divide the whole domain into nine regions. For the WF regions, Regions 1, 2, and 3 are solely determined by the leading edge and essentially equivalent to Regions I, II, and III in the plate case. For the WR regions, Region 4 and Region 6 are out of Mach cones and thus uniform regions with unsteady Mach waves. Regions 5, 7, and 8 are all secondary wave regions but not purely analogous to Region 2. The upstream perturbation from WF adds complexity to the

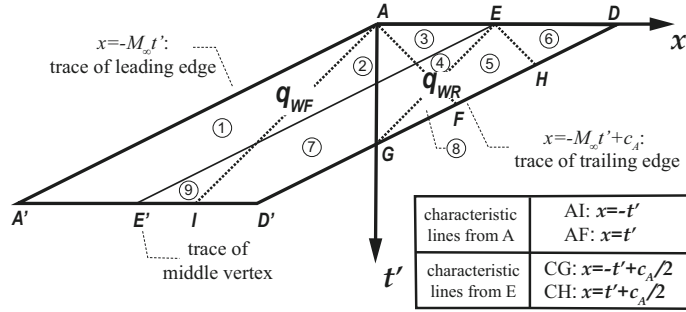


**Fig. 4** Similar to Fig. 2, windward in  $x - t'$  plane can be divided into nine regions

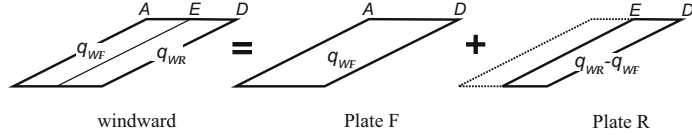


**Fig. 5** The windward can be decomposed into two plates of uniform sources

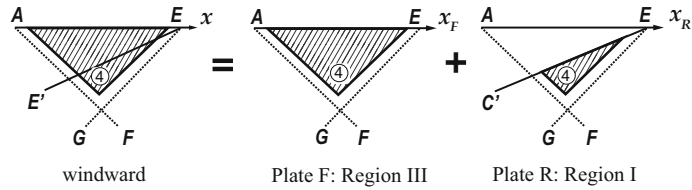


**Fig. 6** The decomposition of Region 4

flow. To specify, Region 5 is influenced by downwash from Region 3, Region 7 forms by the interaction of Region 2 and Mach waves, and Region 8 comes from the interaction of Region 5 and Region 7. Notably, at larger  $M_\infty$ , Region 8 may disappear in case that Region 5 detaches before Region 7 catches up.

To obtain solutions, we should have solved Eq. (1) directly. However, we use an alternative way to simplify the derivation. In fact, the diamond airfoil can be decomposed into two plates, each with uniform source. The pressure coefficient at any point can thus be expressed with the superpositions of plate solutions (Eqs. (2, 4)). We take the windward for example, to detail the derivation process. As shown in Fig. 5, the windward can be decomposed into Plate F and Plate R. Plate F is of full chord length with AoA =  $\alpha_{WF}$ , and Plate R is of half chord length with AoA =  $(\alpha_{WR} - \alpha_{WF})$ .

For Region 4, shown in Fig. 6, its decomposition on the two plates is Regions I and III. Thus, the pressure coefficient in Region 4 is:

$$\begin{aligned} Cp_4^{(W)} &= Cp^{(II)}(\alpha_{WF}) + Cp^{(I)}(\alpha_{WR} - \alpha_{WF}) \\ &= Cp^{(III)}(\alpha_{WF}) + Cp^{(I)}(\alpha_{WR}) - Cp^{(I)}(\alpha_{WF}) \\ &= \frac{2\alpha_{WF}}{M_\infty} + \frac{2\alpha_{WR}}{\sqrt{M_\infty^2 - 1}} - \frac{2\alpha_{WF}}{\sqrt{M_\infty^2 - 1}}. \end{aligned} \quad (8)$$

For Region 8, its decomposition on both plates is Region II, as illustrated in Fig. 7. The pressure coefficient contributed by Plate F is:

$$\begin{aligned} Cp_8^{(WF)} &= Cp^{(II)}(\alpha_{WF}) \\ &= Cp^{(I)}(\alpha_{WF}) \frac{1}{\pi} \arccos \eta_F + Cp^{(III)}(\alpha_{WF}) \frac{1}{\pi} \left( \frac{\pi}{2} + \arcsin \xi_F \right) \\ &= Cp_1^{(W)} \frac{1}{\pi} \arccos \eta_F + Cp_3^{(W)} \frac{1}{\pi} \left( \frac{\pi}{2} + \arcsin \xi_F \right). \end{aligned} \quad (9)$$

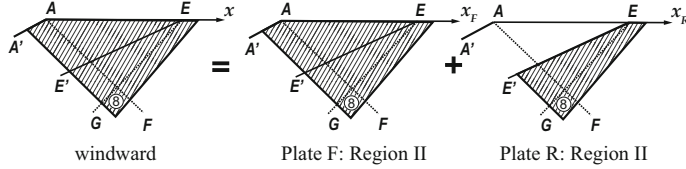


**Fig. 7** The decomposition of Region 8

**Table 2** Linear solution to the windward

Region	Pressure coefficient
Region 1	$Cp_1^{(W)} = \frac{2\alpha_{WF}}{\sqrt{M_\infty^2 - 1}}$
Region 2	$Cp_2^{(W)} = Cp_1^{(W)} \frac{1}{\pi} \arccos \eta_F^{(W)} + Cp_3^{(W)} \frac{1}{\pi} \left( \frac{\pi}{2} + \arcsin \xi_F^{(W)} \right)$
Region 3	$Cp_3^{(W)} = \frac{2\alpha_{WF}}{M_\infty}$
Region 4	$Cp_4^{(W)} = \frac{2\alpha_{WF}}{M_\infty} + \frac{2\alpha_{WR}}{\sqrt{M_\infty^2 - 1}} - \frac{2\alpha_{WF}}{\sqrt{M_\infty^2 - 1}}$
Region 5	$Cp_5^{(W)} = Cp_3^{(W)} + (Cp_4^{(W)} - Cp_3^{(W)}) \frac{1}{\pi} \arccos \eta_R^{(W)} + (Cp_6^{(W)} - Cp_3^{(W)}) \frac{1}{\pi} \left( \frac{\pi}{2} + \arcsin \xi_R^{(W)} \right)$
Region 6	$Cp_6^{(W)} = \frac{2\alpha_{WR}}{M_\infty}$
Region 7	$Cp_7^{(W)} = (Cp_4^{(W)} - Cp_3^{(W)}) + Cp_3^{(W)} \frac{1}{\pi} \left( \frac{\pi}{2} + \arcsin \xi_F^{(W)} \right) + (Cp_9^{(W)} - Cp_4^{(W)} + Cp_3^{(W)}) \frac{1}{\pi} \arccos \eta_F^{(W)}$
Region 8	$Cp_8^{(W)} = Cp_1^{(W)} \frac{1}{\pi} \arccos \eta_F^{(W)} + Cp_3^{(W)} \frac{1}{\pi} \left( \frac{\pi}{2} + \arcsin \xi_F^{(W)} \right) + (Cp_9^{(W)} - Cp_1^{(W)}) \frac{1}{\pi} \arccos \eta_R^{(W)}$ $+ (Cp_6^{(W)} - Cp_3^{(W)}) \frac{1}{\pi} \left( \frac{\pi}{2} + \arcsin \xi_R^{(W)} \right)$
Region 9	$Cp_9^{(W)} = \frac{2\alpha_{WR}}{\sqrt{M_\infty^2 - 1}}$

Here,  $\eta_F$  and  $\xi_F$  are based on Coord F, whose expressions are given by Eq. (5);  $Cp_1^{(W)} = Cp^{(I)}(\alpha_{WF})$ , and  $Cp_3^{(W)} = Cp^{(III)}(\alpha_{WF})$ .

For Plate R, to use Heaslet's solution directly, we adopt Coord R:

$$\begin{aligned}
 Cp_8^{(WR)} &= Cp^{(II)}(\alpha_{WR} - \alpha_{WF}) \\
 &= (Cp^{(I)}(\alpha_{WR}) - Cp^{(I)}(\alpha_{WF})) \frac{1}{\pi} \arccos \eta_R \\
 &\quad + (Cp^{(III)}(\alpha_{WR}) - Cp^{(III)}(\alpha_{WF})) \frac{1}{\pi} \left( \frac{\pi}{2} + \arcsin \xi_R \right) \\
 &= (Cp_9^{(W)} - Cp_1^{(W)}) \frac{1}{\pi} \arccos \eta_R + (Cp_6^{(W)} - Cp_3^{(W)}) \frac{1}{\pi} \left( \frac{\pi}{2} + \arcsin \xi_R \right).
 \end{aligned} \tag{10}$$

Here,  $\eta_R$  and  $\xi_R$  are given by Eq. (5);  $Cp_6^{(W)} = Cp^{(III)}(\alpha_{WR})$ ,  $Cp_9^{(W)} = Cp^{(I)}(\alpha_{WF}) + Cp^{(I)}(\alpha_{WR} - \alpha_{WF})$ . Adding Eqs. (9) and (10), we get the final expression for  $Cp_8^{(W)}$ :

$$\begin{aligned}
 Cp_8^{(W)} &= Cp_8^{(WF)} + Cp_8^{(WR)} \\
 &= Cp_1^{(W)} \frac{1}{\pi} \arccos \eta_F + Cp_3^{(W)} \frac{1}{\pi} \left( \frac{\pi}{2} + \arcsin \xi_F \right) \\
 &\quad + (Cp_9^{(W)} - Cp_1^{(W)}) \frac{1}{\pi} \arccos \eta_R + (Cp_6^{(W)} - Cp_3^{(W)}) \frac{1}{\pi} \left( \frac{\pi}{2} + \arcsin \xi_R \right).
 \end{aligned} \tag{11}$$

For the rest regions, the derivation processes are similar. We list the solutions in Table 2, not shown in detail anymore. As for leeward, replacing  $\alpha_{WF}$  and  $\alpha_{WR}$  with  $\alpha_{LF}$  and  $\alpha_{LR}$  gives its linear solutions.

#### 4 Nonlinear supersonic indicial response of diamond airfoils

With the increase in AoA, nonlinear waves replace Mach waves. We thus distinguish the flow structure first. Noting that the interaction between front flows and Prandtl–Meyer waves at the middle vertex has crucial

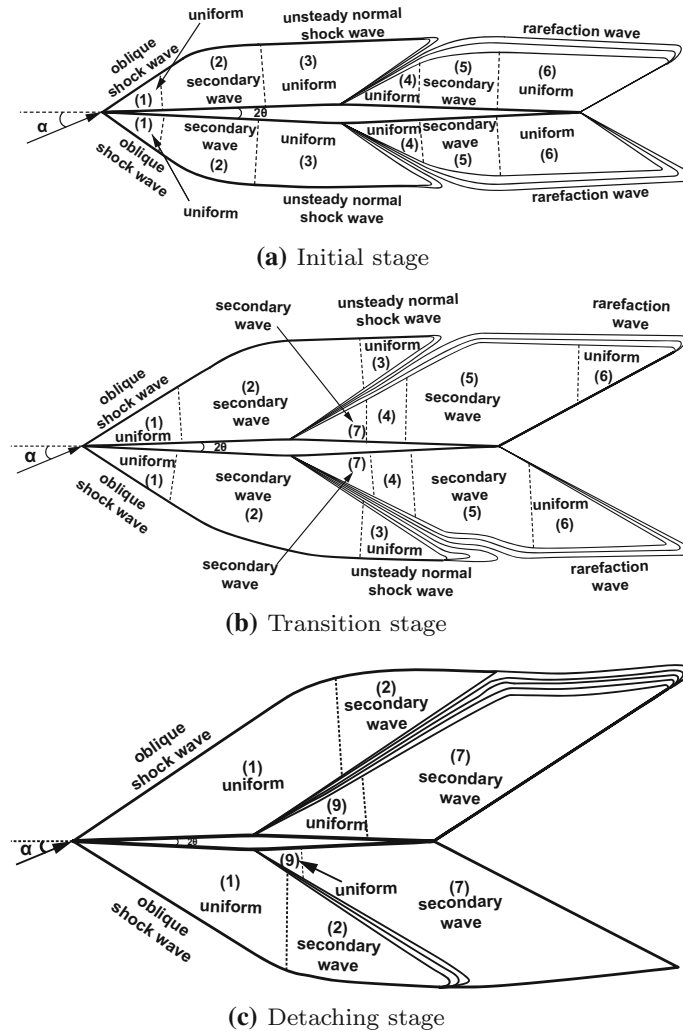


**Fig. 8** Flow structures for  $\alpha < \theta$

influence on rear flows we accordingly divide the process into three stages. At last, we nonlinearly correct the linear solution for each region at the three stages, giving nonlinear indicial response.

#### 4.1 Flow structures of the nonlinear case

In Figs. 8 and 9, we demonstrate the flow structures when  $\alpha < \theta$  and when  $\alpha > \theta$ . Different flow structures in LF and WR arise as a result of the relative size of  $\alpha$  and  $\theta$ . According to the states of secondary waves, we divide the whole starting process of each side into three stages—initial stage, transition stage, and detaching stage. We shall discuss them in detail as follows.

##### 4.1.1 Initial stage

In this stage, the right boundary of Region 2 has not reached the middle vertex yet. Two complete secondary wave regions (Regions 2 and 5) exist on each side. Prandtl–Meyer waves are observed at the middle vertices. Uniform flow in Region 3 goes through Prandtl–Meyer waves and leads to the uniform Region 4.

For  $\alpha < \theta$ , as shown in Fig. 8a, the rest uniform regions on the windward and leeward are both enclosed by an oblique shock wave (Region 1), unsteady normal shock wave (Region 3), and unsteady normal rarefaction wave (Region 6).

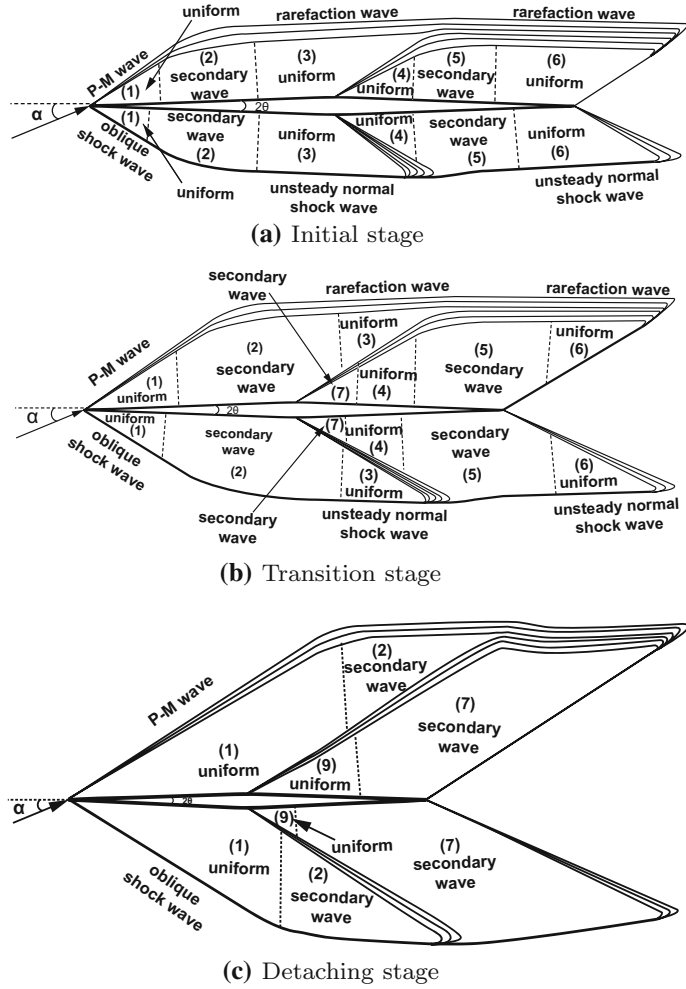


**Fig. 9** Flow structures for  $\alpha > \theta$

For  $\alpha > \theta$ , as shown in Fig. 9a, the uniform regions on the windward are covered by an oblique shock wave (Region 1) and an unsteady normal shock wave (Regions 3 and 6); the uniform regions on the leeward are enclosed by a Prandtl–Meyer wave (Region 1) and unsteady normal rarefaction wave (Region 3 and Region 6).

#### 4.1.2 Transition stage

In the transition stage illustrated by Figs. 8b and 9b, Region 2 is going through the middle vertex. It interacts with Prandtl–Meyer waves, leading to a new secondary wave region—Region 7. At the rear, part of Region 5 is leaving the airfoil. When  $M_\infty$  is not large, Region 7 is likely to catch up with Region 5. Thus, Region 4 vanishes, and Region 8 arises as a result of interaction between Regions 5 and 7.

#### 4.1.3 Detaching stage

In this stage, Region 2 has entirely entered the rear. Region 1 takes up the entire front part (see Figs. 8c, 9c), and uniform Region 9 appears right after Prandtl–Meyer waves at the middle vertices. As secondary regions in the rear part detach, the airfoil comes to a steady state.

## 4.2 Nonlinear correction

To perform nonlinear correction for linear solutions, we introduce some premises for secondary wave regions as follows. These are also adopted by Bai and Wu [10] in the plate case.

**Table 3** Windward

Region	Flow structure	Upstream A	Downstream B	$\alpha_d$ (Deflection angle)
Region 1	Oblique shock wave	$(\rho_\infty, p_\infty, M_\infty)$	$(\rho_1, p_1, M_1)$	$\alpha + \theta$
Region 3	Unsteady normal shock wave	$(\rho_\infty, p_\infty, M_\infty)$	$(\rho_3, p_3, M_3)$	$\alpha + \theta$
Region 4	Prandtl–Meyer wave	$(\rho_3, p_3, M_3)$	$(\rho_4, p_4, M_4)$	$2\theta$
Region 6	$\alpha < \theta$ : unsteady rarefaction wave $\alpha > \theta$ : unsteady normal shock wave	$(\rho_\infty, p_\infty, M_\infty)$	$(\rho_6, p_6, M_6)$	$ \alpha - \theta $
Region 9	Prandtl–Meyer wave	$(\rho_1, p_1, M_1)$	$(\rho_9, p_9, M_9)$	$2\theta$

**Table 4** Leeward

Region	Flow structure	Upstream A	Downstream B	$\alpha_d$ (Deflection angle)
Region 1	$\alpha < \theta$ : oblique shock wave $\alpha > \theta$ : Prandtl–Meyer wave	$(\rho_\infty, p_\infty, M_\infty)$	$(\rho_1, p_1, M_1)$	$ \alpha - \theta $
Region 3	$\alpha < \theta$ : unsteady normal shock wave $\alpha > \theta$ : unsteady rarefaction wave	$(\rho_\infty, p_\infty, M_\infty)$	$(\rho_3, p_3, M_3)$	$ \alpha - \theta $
Region 4	Prandtl–Meyer wave	$(\rho_3, p_3, M_3)$	$(\rho_4, p_4, M_4)$	$2\theta$
Region 6	Unsteady rarefaction wave	$(\rho_\infty, p_\infty, M_\infty)$	$(\rho_6, p_6, M_6)$	$\alpha + \theta$
Region 9	Prandtl–Meyer wave	$(\rho_1, p_1, M_1)$	$(\rho_9, p_9, M_9)$	$2\theta$

- (i) Secondary wave regions' pressure coefficients at the boundaries are in line with those of adjacent uniform regions.
- (ii) The speeds of boundaries are compatible with the characteristic wave speed in their adjacent uniform regions, i.e., the speed of the left boundary is given by the left-going characteristic wave speed  $u_l - a_l$ , and the speed of the right boundary is given by the right-going characteristic wave speed  $u_r + a_r$ .
- (iii) Pressure in secondary wave regions has the same expressions in both linear case and nonlinear case.

#### 4.2.1 Analytical solutions to uniform regions

Regions 1, 3, 4, 6, and 9 are both uniform regions and have definite analytical solutions. Here for brevity, we list their flow structures and related quantities in Tables 3 and 4. One can use these quantities to obtain solutions to each region, via nonlinear wave solutions in the “Appendix.”

#### 4.2.2 The correction of boundaries of secondary wave regions

In this Section, a discussion about windward is given in detail. (Leeward correction could be attained analogously.) For consistency, the following boundaries are all given by Coord F.

For the secondary wave Region 5, its boundaries are given by:

$$\begin{cases} xl_F^{(W5)} = (U_4^{(W)} - a_4^{(W)}) t \cdot \cos \theta + c_A/2 \\ xr_F^{(W5)} = (U_6^{(W)} + a_6^{(W)}) t \cdot \cos \theta + c_A/2 \end{cases} \quad (12)$$

Notably, when applied to Table 5, Eq. (12) should be converted to Coord R:

$$\begin{cases} xl_R^{(W5)} = (U_4^{(W)} - a_4^{(W)}) t \cdot \cos \theta \\ xr_R^{(W5)} = (U_6^{(W)} + a_6^{(W)}) t \cdot \cos \theta \end{cases} \quad (\text{in coord R}). \quad (13)$$

For Regions 2 and 7, the Prandtl–Meyer wave at the middle vertex significantly changes the speed of the boundaries. Thus three stages in Sect. 4.1 should be considered. The demarcation instants of them are  $t_1^{(W)} = \frac{c_A/2}{u_3^{(W)} + a_3^{(W)}}$ , when the right boundary of Region 2 reaches the middle vertex, and  $t_2^{(W)} = \frac{c_A/2}{u_1^{(W)} - a_1^{(W)}}$ , when the left boundary of Region 2 reaches the middle vertex.

When  $t < t_1^{(W)}$ , only complete Region 2 is on the WF, whose boundaries are given by:

$$\begin{cases} xl_F^{(W2)} = (U_1^{(W)} - a_1^{(W)}) t \cdot \cos \theta \\ xr_F^{(W2)} = (U_3^{(W)} + a_3^{(W)}) t \cdot \cos \theta \end{cases} \quad (14)$$

When  $t_1^{(W)} \leq t < t_2^{(W)}$ , Region 2 and Region 7 coexist. Region 2's boundaries are still given by Eq. (14). For Region 7, to accord with Region 2, the speed of its left boundary remains  $u_1^{(W)} - a_1^{(W)}$ . And the speed of its right boundary is updated to  $u_4^{(W)} + a_4^{(W)}$ . Thus, Region 7 is bounded by:

$$\begin{cases} xl_F^{(W7)} = (U_1^{(W)} - a_1^{(W)}) t \cdot \cos \theta \\ xr_F^{(W7)} = (U_4^{(W)} + a_4^{(W)}) (t - t_1^{(W)}) \cdot \cos \theta + c_A/2 \end{cases} . \quad (15)$$

When  $t \geq t_2^{(W)}$ , Region 2 vanishes. The left boundary of Region 7 is updated to  $u_9^{(W)} - a_9^{(W)}$ . We thus get:

$$\begin{cases} xl_F^{(W7)} = (U_9^{(W)} - a_9^{(W)}) (t - t_2^{(W)}) \cdot \cos \theta + c_A/2 \\ xr_F^{(W7)} = (U_4^{(W)} + a_4^{(W)}) (t - t_1^{(W)}) \cdot \cos \theta + c_A/2 \end{cases} . \quad (16)$$

#### 4.2.3 Nonlinear results

Substituting nonlinear pressure of uniform regions and boundaries for linear ones in Table 2, we obtain nonlinear solutions. A summary is provided in Tables 5 and 6.

## 5 Validation via CFD

In this Section, a diamond airfoil with thickness ratio 0.04 ( $\theta = 2.29^\circ$ ) is chosen as the test case. Several combinations of Mach number and AoA are adopted to validate the applicability of our model.

Here, a dimensionless parameter  $\tau = V_\infty t/c_A$  is adopted, which measures the traveled distance of the airfoil.

**Table 5** Nonlinearly corrected solutions for windward

Region	Pressure coefficient
Region 2	$Cp_2^{(W)} = Cp_1^{(W)} \frac{1}{\pi} \arccos \eta_F^{(W2)} + Cp_3^{(W)} \frac{1}{\pi} \left( \frac{\pi}{2} + \arcsin \xi_F^{(W2)} \right)$
Region 5	$Cp_5^{(W)} = Cp_3^{(W)} + (Cp_4^{(W)} - Cp_3^{(W)}) \frac{1}{\pi} \arccos \eta_R^{(W5)} + (Cp_6^{(W)} - Cp_3^{(W)}) \frac{1}{\pi} \left( \frac{\pi}{2} + \arcsin \xi_R^{(W5)} \right)$
Region 7	$Cp_7^{(W)} = (Cp_4^{(W)} - Cp_3^{(W)}) + Cp_3^{(W)} \frac{1}{\pi} \left( \frac{\pi}{2} + \arcsin \xi_F^{(W7)} \right) + (Cp_9^{(W)} - Cp_4^{(W)} + Cp_3^{(W)}) \frac{1}{\pi} \arccos \eta_F^{(W7)}$
Region 8	$Cp_8^{(W)} = Cp_1^{(W)} \frac{1}{\pi} \arccos \eta_F^{(W7)} + Cp_3^{(W)} \frac{1}{\pi} \left( \frac{\pi}{2} + \arcsin \xi_F^{(W7)} \right) + (Cp_9^{(W)} - Cp_1^{(W)}) \frac{1}{\pi} \arccos \eta_R^{(W5)}$ $+ (Cp_6^{(W)} - Cp_3^{(W)}) \frac{1}{\pi} \left( \frac{\pi}{2} + \arcsin \xi_R^{(W5)} \right)$

**Table 6** Nonlinearly corrected solutions for leeward

Region	Pressure coefficient
Region 2	$Cp_2^{(L)} = Cp_1^{(L)} \frac{1}{\pi} \arccos \eta_F^{(L2)} + Cp_3^{(L)} \frac{1}{\pi} \left( \frac{\pi}{2} + \arcsin \xi_F^{(L2)} \right)$
Region 5	$Cp_5^{(L)} = Cp_3^{(L)} + (Cp_4^{(L)} - Cp_3^{(L)}) \frac{1}{\pi} \arccos \eta_R^{(L5)} + (Cp_6^{(L)} - Cp_3^{(L)}) \frac{1}{\pi} \left( \frac{\pi}{2} + \arcsin \xi_R^{(L5)} \right)$
Region 7	$Cp_7^{(L)} = (Cp_4^{(L)} - Cp_3^{(L)}) + Cp_3^{(L)} \frac{1}{\pi} \left( \frac{\pi}{2} + \arcsin \xi_F^{(L7)} \right) + (Cp_9^{(L)} - Cp_4^{(L)} + Cp_3^{(L)}) \frac{1}{\pi} \arccos \eta_F^{(L7)}$
Region 8	$Cp_8^{(L)} = Cp_1^{(L)} \frac{1}{\pi} \arccos \eta_F^{(L7)} + Cp_3^{(L)} \frac{1}{\pi} \left( \frac{\pi}{2} + \arcsin \xi_F^{(L7)} \right) + (Cp_9^{(L)} - Cp_1^{(L)}) \frac{1}{\pi} \arccos \eta_R^{(L5)}$ $+ (Cp_6^{(L)} - Cp_3^{(L)}) \frac{1}{\pi} \left( \frac{\pi}{2} + \arcsin \xi_R^{(L5)} \right)$

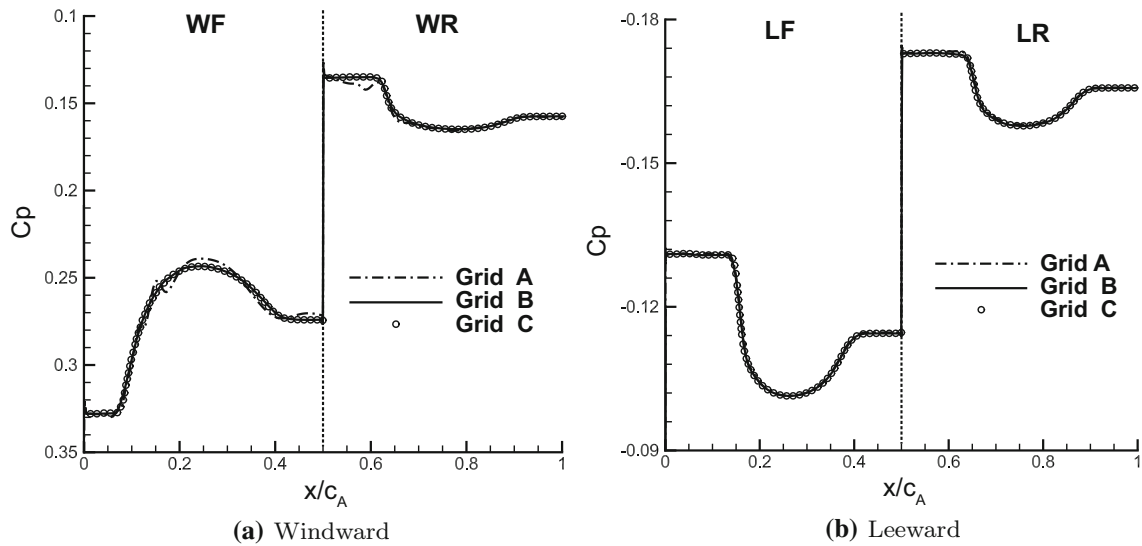


**Fig. 10** Pressure distribution given by three different grids, calculated at  $M_\infty = 2$ ,  $\alpha = 10^\circ$ , and  $\theta = 2.29^\circ$

### 5.1 CFD method and grid-independent study

The CFD simulations are performed by ANSYS Fluent. The second-order upwind scheme for spatial discretization and the AUSM scheme for flux are adopted. Three grids are chosen for the grid-independent study, labeled with A, B, and C, from the coarsest to the finest. Grid A has 201 nodes along the chord and is composed of 114,300 elements in total. Grid B is the medium one, with 301 nodes along the chord and 265,000 elements in total. As for Grid C, 401 nodes are distributed along the chord, and 412,000 elements comprise the entire computational domain. Figure 10 displays the results obtained by Grid A, Grid B, and Grid C. It can be seen that there are significant numerical oscillations in Grid A's results (dash-dot line), while Grid B (solid line) and Grid C (circle) almost give the same results. Taking a balance between efficiency and effectivity, we select Grid B for the following numerical computation.

### 5.2 Pressure distribution along surfaces

To proffer a comprehensive validation, we choose representative instants of each test case, which demonstrate the three stages in Sect. 4.1.

Figures 11 and 12 display the comparison between linear results and CFD results, at  $\text{AoA} = 1^\circ, 5^\circ$ , and  $10^\circ$ . For  $\text{AoA} = 1^\circ$ , nonlinearity is not too prominent, and the linear results agree with CFD results in most parts of the airfoil, except WF. In fact, the equivalent AoA of WF is  $3.29^\circ$ , which is beyond the scope of linear theory. With AoA increasing to  $5^\circ$  and  $10^\circ$ , the linear results deviate significantly from CFD results. The error reaches 70% at largest.

The identical test cases are also used to validate the nonlinear model. Figures 13 and 14 illustrate the comparison of pressure distribution. It can be seen that the nonlinear correction significantly improves the original linear results. The estimated pressure distribution in uniform regions is fairly accurate. As for the secondary wave regions, the boundaries of secondary wave regions are correctly predicted. The discrepancy of pressure distribution is largely reduced, and the predicted results are much more acceptable. Even for  $\alpha = 10^\circ$ , the relative error is not larger than 13%.

For  $M_\infty = 4$  case, Region 8 is absent because of high Mach number. To complete the validation, a comparison at  $M_\infty = 2$  is carried out. Figure 15 displays the chordwise pressure distribution of Region 8. It proves our model's accuracy in Region 8 as well as in other regions.

### 5.3 Force evolution in normal and axial direction

Finally, we validate aerodynamical forces. The corresponding normal force coefficient  $C_n$  and axial force coefficient  $C_a$  can be evaluated by integrating each region's pressure. Figure 16 compares the force coefficients by the

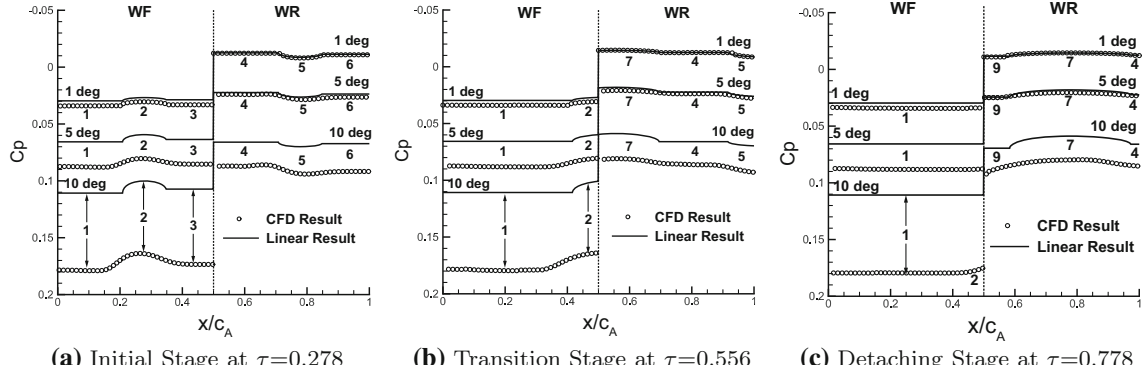


**Fig. 11** Comparison between CFD results and linear results at the windward, calculated at  $M_\infty = 4$  and  $\alpha = 1^\circ, 5^\circ, 10^\circ$

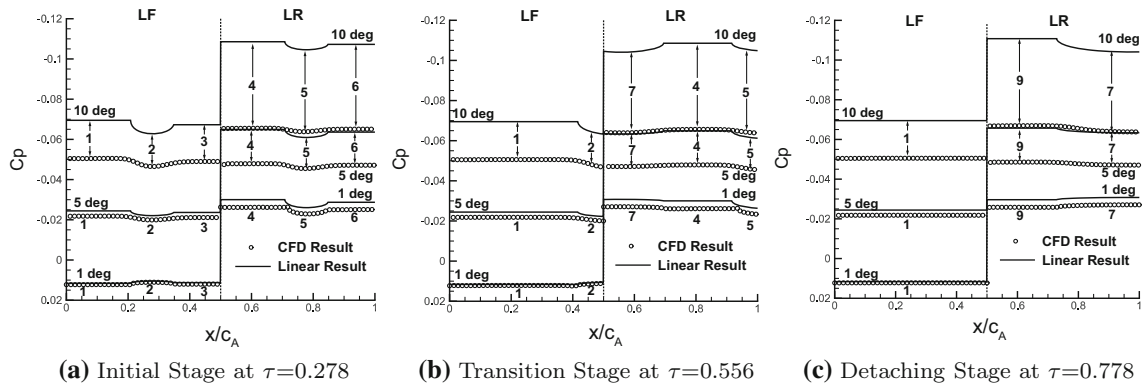


**Fig. 12** Comparison between CFD results and linear results at the leeward, calculated at  $M_\infty = 4$  and  $\alpha = 1^\circ, 5^\circ, 10^\circ$

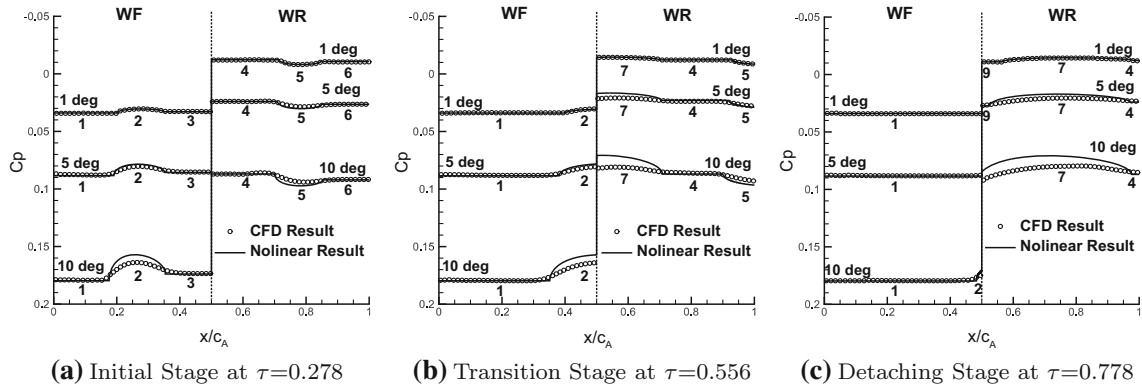


**Fig. 13** Comparison between CFD results and nonlinear results at windward, calculated at  $M_\infty = 4$  and  $\alpha = 1^\circ, 5^\circ, 10^\circ$

linear method, nonlinear correction method, and CFD, for  $M_\infty = 4$  and  $\alpha = 1^\circ, 10^\circ$ . It can be seen that at  $\alpha = 1^\circ$ , the linear method (dash-dot line) could give a nearly good prediction on forces. Its 1% error can be explained by the nonlinearity from thickness. In  $\alpha = 10^\circ$ , the nonlinearity from AoA arises; the inaccuracy of the linear method nonetheless reaches 10% compared with CFD results. For the nonlinear results represented by solid line, it provides a reasonably good estimation of forces instead. It is nonetheless seen that the discrepancy cannot be satisfactorily eliminated. This error is to blame for current models' inaccuracy in the secondary wave regions.

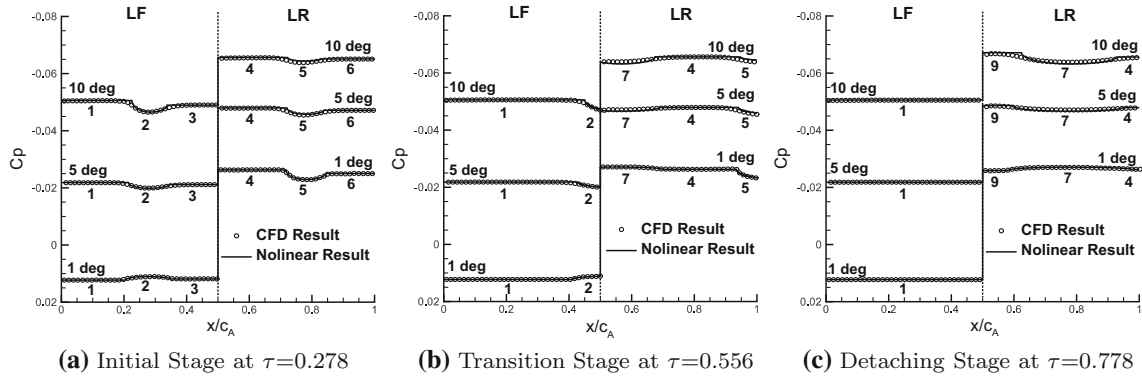


**Fig. 14** The comparison between CFD results and nonlinear results at leeward, calculated at  $M_\infty = 4$  and  $\alpha = 1^\circ, 5^\circ, 10^\circ$

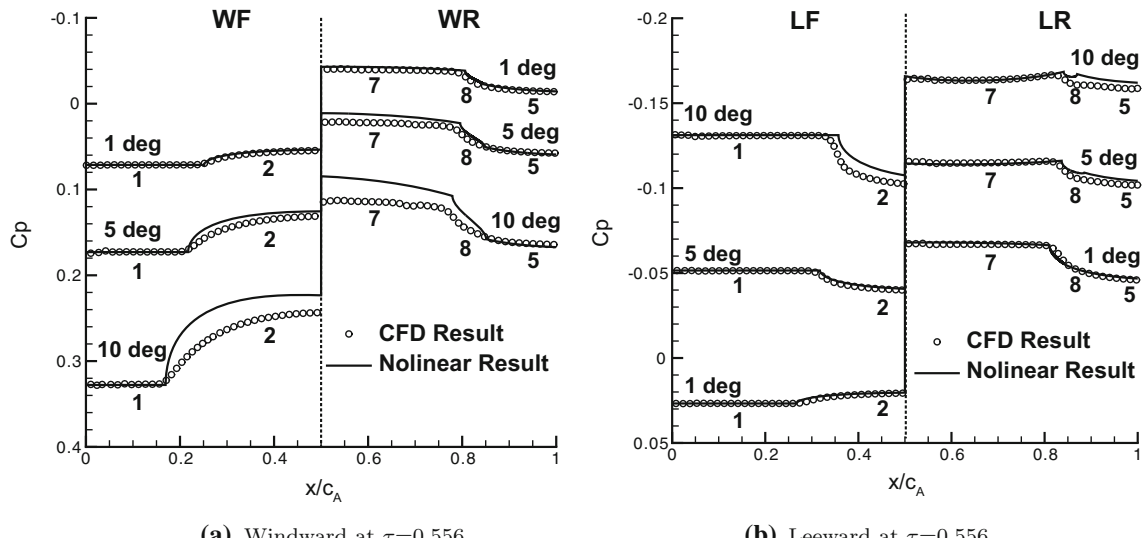


**Fig. 15** The comparison between nonlinear results and CFD results for Region 8, calculated at  $M_\infty = 2$  and  $\alpha = 1^\circ, 5^\circ, 10^\circ$

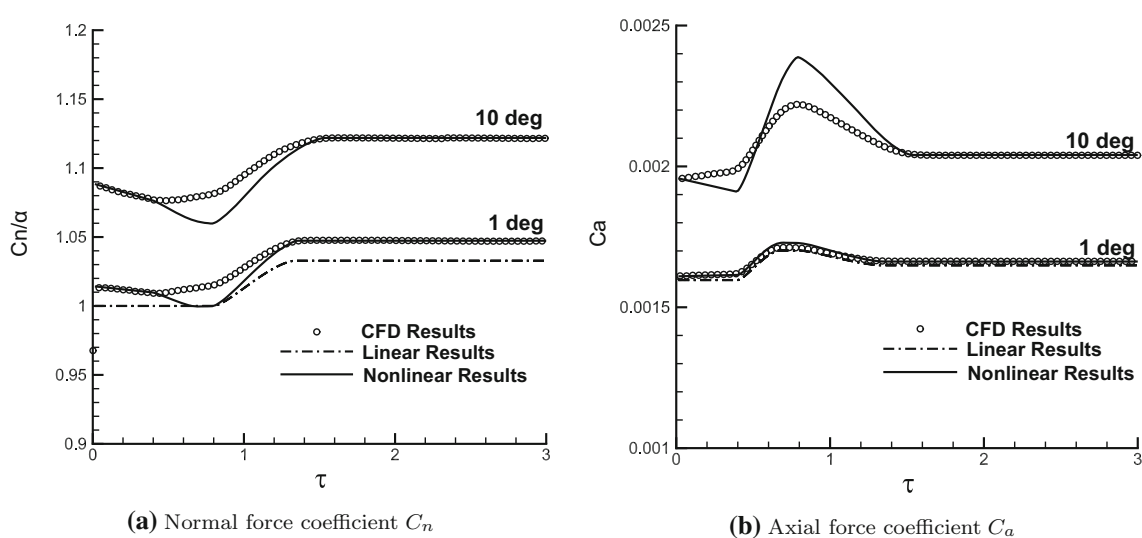


**Fig. 16** The comparison among linear method, nonlinear correction method, and CFD for normal force coefficient  $C_n$  and axial force coefficient  $C_a$ , in  $M_\infty = 4$  and  $\alpha = 1^\circ, 10^\circ$

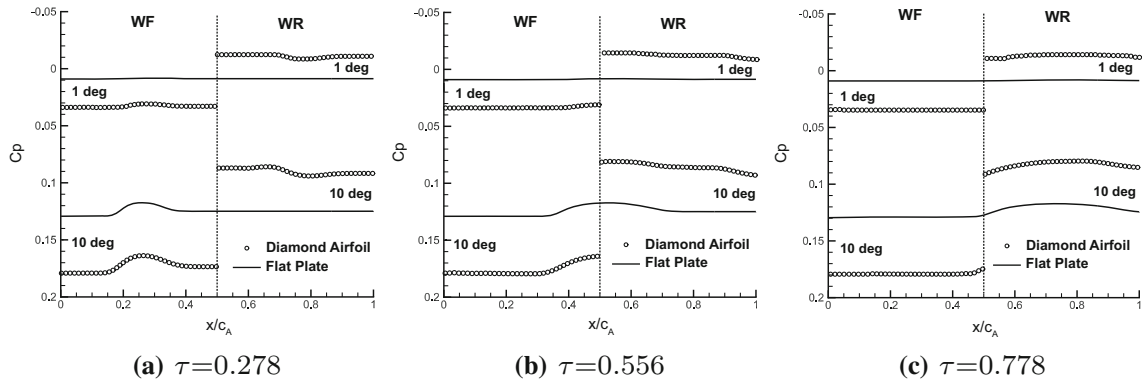


**Fig. 17** The comparison of windward CFD results between diamond airfoil and flat plate, calculated at  $M_\infty = 4$  and  $\alpha = 1^\circ, 10^\circ$

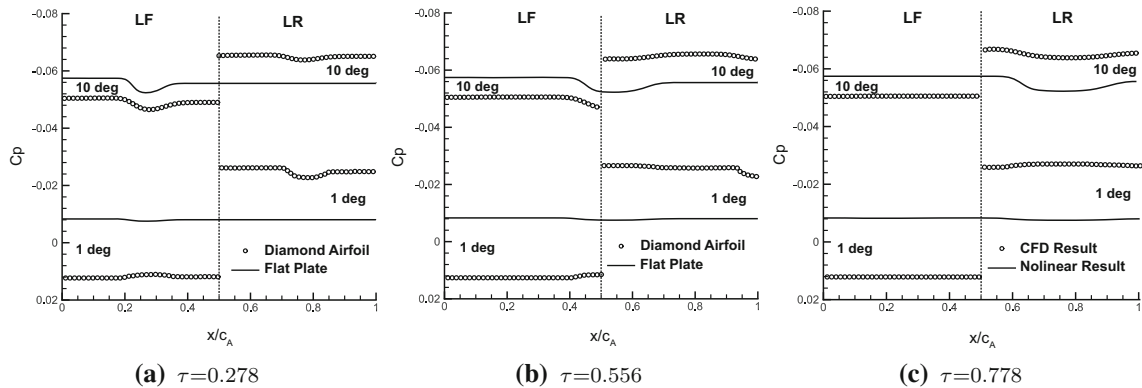


**Fig. 18** The comparison of leeward CFD results between diamond airfoil and flat plate, calculated at  $M_\infty = 4$  and  $\alpha = 1^\circ, 10^\circ$

#### 5.4 The effect of airfoil thickness

Here, we offer a closer view of the effect of thickness. A diamond airfoil and a flat plate with the same chord length are chosen. The step motion is set at  $M_\infty = 4$  and  $\alpha = 1^\circ, 10^\circ$ . Figures 17 and 18 illustrate their pressure distribution at the same instants, and aerodynamic forces are displayed in Fig. 19. It can be seen that airfoil thickness has important influence on the aerodynamic forces. Compared with a flat plate at the same angle of attack, the diamond airfoil has larger AoA at WF and LR and smaller AoA at WR and LF. As a result, higher pressure coefficient in the WF and LF, and lower pressure coefficient in the WR and LR are observed.

As for force evolution, a flat plate only contains two stages during the evolution, i.e., the initial stage and the detaching stage. Although Regions I on both sides combine to produce larger pressure difference and their coverage areas increase over time, a plateau of  $C_n$  in the initial stage is observed. It is because secondary wave regions offset this pressure difference. In fact, secondary wave regions produce a lower pressure coefficient at the windward and a higher pressure coefficient at the leeward. As for the detaching stage, since the secondary wave regions start to detach, this offsetting effect subsides, and  $C_n$  gradually rises to the final steady state.

For diamond airfoils,  $C_n$  nonetheless decreases at the initial stage. This is due to that the equivalent AoA of WF is larger than that of LF. The pressure drop in Region 2 of WF thus cannot be eliminated by the pressure rise in Region 2 of LF. Then in the transition stage, Regions 2 and 5 vanish and Region 7 forms. Unlike Region 2, Region 7's pressure coefficient is not so distinct from adjacent regions. Thus, a recovery of  $C_n$  can be seen. Finally, at the detaching stage,  $C_n$  increases dramatically, similar to a flat plate, and finally reaches a little higher amount.

For  $C_a$ , it is a direct consequence of thickness.  $C_a$  slightly increases at the initial stage, for the front experiences stronger compression than the rear, and this inequality accumulates as secondary wave regions expand. Then in the transition stage,  $C_a$  increases drastically and an overshoot is observed, for Region 7 has the lower pressure coefficient. Finally, in the detaching stage, Region 7 detaches and  $C_a$  drops to a constant amount.

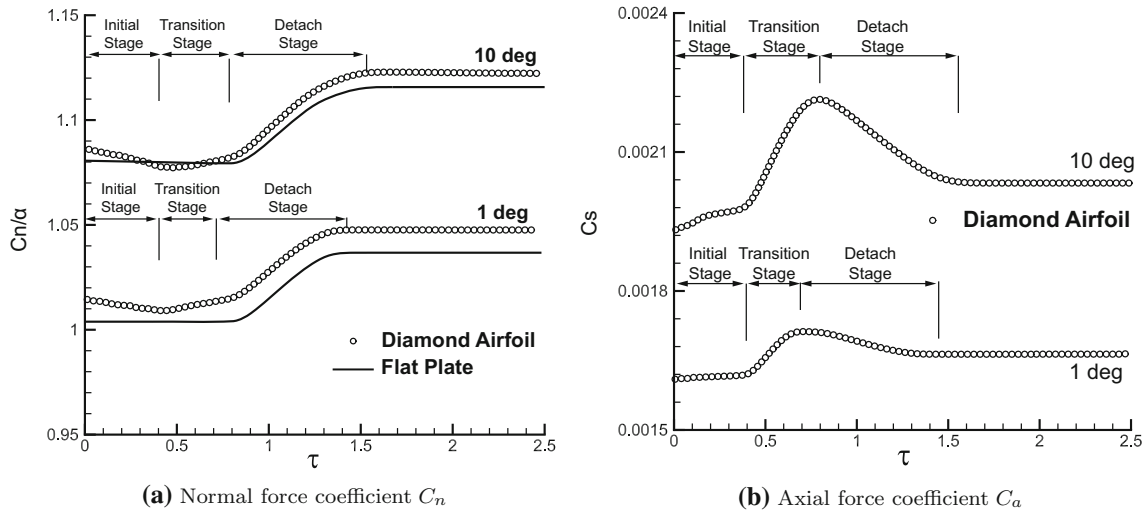


**Fig. 19** The comparison of CFD results of aerodynamic force between diamond airfoil and flat plate, calculated at  $M_\infty = 4$  and  $\alpha = 1^\circ, 10^\circ$

## 6 Conclusions

The supersonic indicial response of a diamond airfoil is investigated. A nonlinear model is analytically present in this paper, accounting for effects of large-amplitude motion and airfoil thickness. This model is capable of predicting the pressure distribution, wave speed, and indicial force at any instant. Below are the main conclusions of this paper.

1. After step motion, nine regions, on each side, are found in both linear cases and nonlinear cases. Among them, five regions are uniform and covered by definite waves. The rest are secondary wave regions, all nonuniform and time-varying. These secondary wave regions have broader causes than those of a flat plate. Upstream flow, interaction between Mach waves and secondary waves, and interaction between secondary waves are also responsible for the formation.
2. For the linear case, each side of a diamond airfoil can be regarded as a combination of two plates. Heaslet and Lomax's solution [7] can be applied to each plate. The linear indicial response of a diamond airfoil can be attained by superposing that of each plate. CFD simulation attests the accuracy of this linear model at small AoA.
3. For the nonlinear case, nonlinear waves—steady and unsteady shock waves, steady and unsteady rarefaction waves—replace original Mach waves. Details are shown in Figs. 8 and 9. According to the relative position of Region 2 and middle vertex, the nonlinear indicial response can be divided into three stages, i.e., the initial stage, the transition stage, and the detaching stage.
4. An analytical nonlinear model is proposed. The pressure in the uniform regions is accurately given by classical theories. As for secondary wave regions, the boundaries are separately determined according to each stage. To bridge the linear case and the nonlinear case, the analogous pressure distribution is assumed. In contrast to numerical results, this nonlinear model demonstrates fairly good estimation, covering a wide range of Mach numbers and angles of attack.
5. The aerodynamic force evolution is found in line with three stages. In the initial stage,  $C_n$  drops, and  $C_a$  slightly increases; in the transition stage,  $C_n$  recovers and  $C_a$  largely increases, and an overshoot of  $C_a$  is observed; in the detaching stage,  $C_n$  largely increases to steady state and  $C_a$  decreases to steady state.

The present study is restricted to a diamond airfoil, which is typical for a supersonic airplane. For general airfoil configuration, if we regard its profile as a combination of multiple plates, the current model can be extended without conceptual difficulty. However, describing this indicial response requires large quantities of regions and stages. Even for three plates, around eighteen regions and six stages are needed for each side. The derivation process is arduous, and a simplified model is necessary. Another perspective of future work is to consider three-dimensional effects. The current study of two-dimensional cases allows us to understand the flow physics associated with indicial response. We believe that the three-dimensional effects could be understood as an additional correction to two-dimensional results.

**Acknowledgements** This work is supported by Chinese Postdoc Foundation (No. 2018M640119), by the Natural National Science Foundation of China (No. 11802157), and by Tsinghua Postdoc supporting program. We deeply appreciate Editor and Referees, for their valuable suggestions help improve this manuscript.

## Appendix: Solutions to the uniform regions in the nonlinear situation

1. *Oblique shock wave* Using oblique shock relation, we can get

$$\left\{ \begin{array}{l} \tan \alpha_d = 2 \cot \beta \frac{M_A^2 \sin^2 \beta - 1}{M_A^2 (\gamma + \cos 2\beta) + 2} \\ \rho_B = \rho_A \frac{(\gamma+1) M_A^2 \sin^2 \beta}{2 + (\gamma-1) M_A^2 \sin^2 \beta} \\ (M_B)^2 = \frac{M_A^2 + \frac{2}{\gamma-1}}{\frac{2\gamma}{\gamma-1} M_A^2 \sin^2 \beta - 1} + \frac{M_A^2 \cos^2 \beta}{\frac{\gamma-1}{2} M_A^2 \sin^2 \beta + 1} \\ u_B = M_B \times a_B, a_B = \sqrt{\frac{\gamma p_B}{\rho_B}} \\ p_B = p_A \left( 1 + \frac{2\gamma}{\gamma+1} (M_A^2 \sin^2 \beta - 1) \right) \\ C p_B = \frac{2}{\gamma M_\infty^2} \left( \frac{p_A}{p_\infty} \left( 1 + \frac{2\gamma}{\gamma+1} (M_A^2 \sin^2 \beta - 1) \right) - 1 \right). \end{array} \right. \quad (A.1)$$

Here  $\beta$  is the shock angle with respect to  $\alpha_d$  and  $M_\infty$ .

2. *Unsteady normal shock wave* We use  $M_S$  to denote the Mach number of the shock wave. In the step motion, behind unsteady waves are airfoil surfaces. Thus, with  $v_{B,n} = 0$ , the classical solution gives:

$$\left\{ \begin{array}{l} M_S = \frac{\gamma+1}{4} M_A \sin \alpha_r + \sqrt{1 + \left( \frac{\gamma+1}{4} M_A \sin \alpha_r \right)^2} \\ \rho_B = \rho_A \frac{M_S^2}{1 + \frac{\gamma-1}{\gamma+1} (M_S^2 - 1)} \\ u_B = u_A \cos \alpha_r, a_B = \sqrt{\frac{\gamma p_B}{\rho_B}} \\ p_B = p_\infty \left( 1 + \frac{2\gamma}{\gamma+1} (M_S^2 - 1) \right) \\ C p_B = \frac{2}{\gamma M_\infty^2} \left( \frac{p_A}{p_\infty} \left( 1 + \frac{\gamma(\gamma+1)}{4} M_A^2 \sin^2 \alpha_r + \gamma \sqrt{M_A^2 \sin^2 \alpha_d + \left( \frac{\gamma+1}{4} M_A^2 \sin^2 \alpha_d \right)^2} \right) - 1 \right). \end{array} \right. \quad (A.2)$$

3. *Prandtl–Meyer wave* Prandtl–Meyer relations give:

$$\left\{ \begin{array}{l} v(M_B) - v(M_A) = \alpha_d \\ v(M) = \sqrt{\frac{\gamma+1}{\gamma-1}} \arctan \left( \sqrt{\frac{\gamma-1}{\gamma+1}} \sqrt{M^2 - 1} \right) - \arctan \sqrt{M^2 - 1} \\ u_B = M_B \times a_B, a_B = \sqrt{\frac{\gamma p_B}{\rho_B}} \\ \rho_B = \rho_A \left( \frac{1 + \frac{1}{2}(\gamma-1) M_A^2}{1 + \frac{1}{2}(\gamma-1) M_B^2} \right)^{\frac{1}{\gamma-1}} \\ p_B = p_A \left( \frac{1 + \frac{1}{2}(\gamma-1) M_A^2}{1 + \frac{1}{2}(\gamma-1) M_B^2} \right)^{\frac{\gamma}{\gamma-1}} \\ C_p = \frac{2\gamma}{M_\infty^2} \left( \frac{p_A}{p_\infty} \left( \frac{1 + \frac{1}{2}(\gamma-1) M_A^2}{1 + \frac{1}{2}(\gamma-1) M_B^2} \right)^{\frac{\gamma}{\gamma-1}} - 1 \right). \end{array} \right. \quad (A.3)$$

**Table 7** Flat plate

Region	Flow structure	Upstream A	Downstream B	$\alpha_d$ (deflection angle)
<i>Windward</i>				
Region I	Oblique shock wave	$(\rho_\infty, p_\infty, M_\infty)$	$(\rho_1, p_1, M_1)$	$\alpha$
Region III	Unsteady normal shock wave	$(\rho_\infty, p_\infty, M_\infty)$	$(\rho_{III}, p_{III}, M_{III})$	$\alpha$
<i>Leeward</i>				
Region I	Prandtl–Meyer wave	$(\rho_\infty, p_\infty, M_\infty)$	$(\rho_1, p_1, M_1)$	$\alpha$
Region III	Unsteady normal rarefaction wave	$(\rho_\infty, p_\infty, M_\infty)$	$(\rho_{III}, p_{III}, M_{III})$	$\alpha$

4. *Unsteady rarefaction wave* Considering  $v_{B,n} = 0$ , the solution is given by isentropic relation:

$$\begin{cases} a_B = a_A - \frac{\gamma-1}{2} V_A \sin \alpha_d \\ \rho_B = \rho_A \left(1 - \frac{\gamma-1}{2} M_A \sin \alpha_d\right)^{\frac{2}{\gamma-1}} \\ p_B = p_A \left(1 - \frac{\gamma-1}{2} M_A \sin \alpha_d\right)^{\frac{2\gamma}{\gamma-1}} \\ C_p = \frac{2}{\gamma M_\infty^2} \left( \frac{p_A}{p_\infty} \left(1 - \frac{\gamma-1}{2} M_A \sin \alpha_d\right)^{\frac{2\gamma}{\gamma-1}} - 1 \right). \end{cases}. \quad (\text{A.4})$$

For plates, the flow structure and flow parameters are given by Table 7. For any uniform region of the flat plate, one can obtain its solution by taking upstream flow parameters into the corresponding nonlinear wave relation.

## References

- Bisplinghoff, R.L., Ashley, H., Halfman, R.L.: Aeroelasticity, pp. 294–375. Addison-Wesley, Reading (1995)
- Mastroddi, F., Stella, F., Cantiani, D., Vetrano, F.: Linearized aeroelastic gust response analysis of a launch vehicle. *J. Spacecr. Rockets* **48**(3), 420–432 (2011)
- Biot, M.A.: Loads on a supersonic wing striking a sharp-edged gust. *J. Aeronaut. Sci.* **16**(5), 296–300 (1949)
- Hernandes, F., Soviero, P.A.D.O.: A numerical model for thin airfoils in unsteady compressible arbitrary motion. *J. Braz. Soc. Mech. Sci. Eng.* **29**(3), 253–261 (2007)
- Choi, S.W., Chang, K.S.: Navier-Stokes computation of a rapidly deploying spoiler. *J. Aircr.* **37**(4), 655–661 (2000)
- Tobak, M., Chapman, G.T., Schiff, L.B.: Mathematical modeling of the aerodynamic characteristics in flight dynamics. In: Proceedings of the Berkeley-Ames Conference on Nonlinear Problems in Control and Fluid Dynamics, vol. 2 (1984)
- Heaslet, M.A., Lomax, H.: Two-dimensional unsteady lift problems in supersonic flight. National Aeronautics and Space Administration Moffett Field CA Ames Research Center (1948)
- Lomax, H., Heaslet, M.A., Fuller, F.B., Sluder, L.: Two-and three-dimensional unsteady lift problems in high-speed flight. Technical Report Archive & Image Library (1952)
- Jaworski, J.W., Dowell, E.H.: Supersonic indicial lift functions from transform methods. *AIAA J.* **45**(8), 2106–2111 (2007)
- Bai, C.Y., Wu, Z.N.: Supersonic indicial response with nonlinear corrections by shock and rarefaction waves. *AIAA J.* **55**(3), 883–893 (2016)
- Bai, C.Y., Wu, Z.N.: Hybrid Riemann/self-similar flow structure by steady-and unsteady-wave interaction. *AIAA J.* **55**(12), 4193–4202 (2017)
- Bai, C.Y., Li, S., Wu, Z.N.: Supersonic starting flow by accelerated sinking movement to large angle of attack. *AIAA J.* **57**(5), 1988–2000 (2019)
- Bai, C.Y., Li, S., Wu, Z.N.: Unsteady supersonic flow for a plate undergoing three-stage sinking motion. *AIAA J.* **58**(1), 1–12 (2019)
- Chavez, F.R., Liu, D.D.: Unsteady unified hypersonic/supersonic method for aeroelastic applications including wave/shock interaction. *AIAA J.* **33**(6), 1090–1097 (1995)